

www.acsami.org Research Article

Large-Area Fabrication of Complex Nanohole Arrays with Highly Tunable Plasmonic Properties

Yanfeng Wang, Harrison B. Chong, Zhengjun Zhang,* and Yiping Zhao*



Cite This: ACS Appl. Mater. Interfaces 2020, 12, 37435-37443



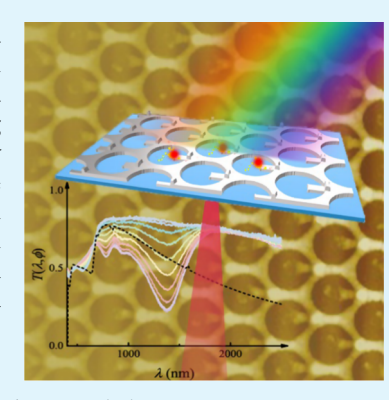
ACCESS

Metrics & More



Supporting Information

ABSTRACT: By combining nanosphere lithography with oblique angle deposition, large-area asymmetric compound Ag nanohole arrays with nanorods inside the hole were patterned on substrates. The technique enabled the production of complex nanohole arrays with controlled hole diameter, thickness, and rod structure inside the hole. The compound asymmetric Ag nanohole structures showed strong polarization-dependent optical properties, and a new extraordinary optical transmission (EOT) mode with tunable resonance wavelength at the near-IR region was observed. The transmission at the new EOT wavelength region can increase from 27% of nanohole to 69% of the compound structure, and these structures can achieve a refractive index sensitivity as high as 847 nm RIU⁻¹. The tunable EOT wavelength and strong polarization-dependent optical properties make the structure ideal for ultrathin optical filters, polarizers, surface-enhanced spectroscopies, etc.



KEYWORDS: extraordinary optical transmission, compound asymmetric nanohole array, nanorod in nanohole, Y-shaped nanorod in nanohole, tunable transmission

INTRODUCTION

In recent years, asymmetric plasmonic structures have attracted considerable attention 1-3 because of their unique optical properties such as strong optical nonlinearity^{4-7*} and Fano resonance, 3,5,8-10 which involve the coupling of continuum states to the discrete state of oscillating systems. In particular, nanohole (NH) arrays with asymmetric hole structures, 11,12 or combined with other asymmetric nanostructures, 1,13 have been widely reported due to their improved structural design freedom and novel optical properties. Among these asymmetric hole arrays, periodic nanorod (NR) and nanohole asymmetric compound structures are of interest. 13-17 NH array structures possess both localized surface plasmon resonance (LSPR) and surface plasmon polaritons (SPPs), while NR arrays exhibit two LSPR modes, i.e., the transverse and longitudinal modes. A combined NR and NH compound asymmetric structure should demonstrate novel optical properties. For example, tilted NRs grown on NH arrays demonstrated strong polarization-dependent optical properties and a new extraordinary optical transmission (EOT) mode in ref 16. The transmission spectrum of NH arrays with tilted NRs grown on them is similar to that of the corresponding plain NH arrays when the incident light polarization is perpendicular to the long axis of the NRs, with two EOT peaks caused by the surface plasmon resonance at the Ag-air and Ag-glass interfaces. When the incident light polarization is parallel to the long axis of the NRs, a new EOT peak appears at a longer wavelength than the normal EOT peaks. This EOT wavelength red-shifts with NR length, demonstrating a tunable

optical property. Furthermore, according to finite difference time domain (FDTD) calculations, 15,17 planar NR in NH (NRinNH) structures also possess strong polarization-dependent optical properties and a new tunable EOT mode but with higher transmission when compared to that of tilted NRs grown on NH structures in ref 16. In addition, an epsilon-nearzero (ENZ) property was also presented at the new EOT resonance wavelength with the same tunability. 15 The local Efields around the NRs are greatly enhanced at the new EOT wavelength, rendering these structures potentially useful for surface-enhanced spectroscopies, such as surface-enhanced Raman scattering and surface-enhanced infrared absorption. 19,20 Experimentally, these structures have been realized with E-beam lithography and focused ion beam lithography. Polarization-dependent optical properties 17,21 and nonlinear optical properties^{4,22,23} have been demonstrated with these methods; however, scanning beam lithography techniques (Ebeam lithography²⁴⁻²⁷ and focused ion beam lithography²⁸⁻³¹) traditionally used to fabricate metasurfaces suffer from high cost, low throughput, and require sophisticated and expensive equipment. These limitations hinder industrial

Received: April 15, 2020 Accepted: July 23, 2020 Published: July 23, 2020





application, inspiring interest in a nanofabrication technique able to mass-produce these complex nanostructures over square centimeter areas at a low cost.

Nanosphere lithography (NSL), which utilizes a selfassembled monolayer of polystyrene nanospheres (PSNSs) on a solid substrate surface to form a mask with subsequent evaporation and/or etching processes to fabricate nanostructure arrays, is now recognized as a low-cost, high throughput, scalable, and reproducible nanofabrication technique. 32,33 This method provides an economical alternative to scanning beam lithography techniques.34 Large-area NH arrays can be fabricated by combining NSL with electron-beam deposition. 35,36 During the deposition, metal vapor flux normal to the substrate condenses into the crevices of the pre-etched PSNS monolayer,³⁷ forming NH structures. By tilting the substrate at the proper angle and using the gap between two nearby nanospheres, NRs can also be fabricated.³⁸ These two steps can be combined to form compound NRinNH structures, which may possess intriguing optical properties.

In this work, we have successfully fabricated large-area asymmetric compound nanorod in nanohole (ACRH) structures by combining NSL and oblique angle deposition (OAD). Aspects of the compound NH array geometry such as the period of the lattice, hole diameter, and rod length can be controlled precisely by varying the size, etching duration of the PSNS, and the tilt angle during the metal deposition, respectively. The resulting compound NH arrays have shown a high degree of optical tunability, strong polarization-dependent optical properties, a new EOT mode, and Fanolike resonances, all of which were predicted by FDTD calculations. The tunability of the plasmonic properties of the ACRH structures was systematically investigated, and the improved sensitivity of these structures for refractive index sensing was also verified experimentally.

■ EXPERIMENTS

Fabrication Procedure for ACRH Structures. Materials. Briefly, 500 and 750 nm PSNSs (Polyscience, Lot# 679675 and Lot# 687640) and ethanol (Sigma-Aldrich, 98%) were used to form the nanosphere monolayers on cleaned glass slides (Gold Seal, Part# 3010). Sulfuric acid (Fisher Scientific, 98%), ammonium hydroxide (Fisher Scientific, 98%), and hydrogen peroxide (Fisher Scientific, 30%) were used to clean the substrates. Silver (Plasmaterials, 99.99%) and titanium pellets (Kurt J. Lesker, 99.995%) were purchased as the evaporation materials. Methanol, acetone, 1-hexanol (Tokyo Chemical Industry Co., >98%), chloroform (J.T. Baker, 99%), tetrachloromethane (Sigma-Aldrich, 99.9%), and toluene (Fisher Scientific, 99.8%) were purchased for refractive index sensing measurements. All chemicals and materials were used without further purification. Deionized water (18 MΩ cm) was used throughout the experiments.

Fabrication of the ACRH Structures. The general fabrication procedure is outlined in Figure 1. Prior to monolayer formation, the glass substrates were cleaned with sulfuric acid, ammonium hydroxide, and hydrogen peroxide. All substrates were then thoroughly rinsed in deionized water. Substrates that were not coated with monolayer were then dried with N_2 gas. The uniform PSNS (diameter L = 500 and 750 nm) monolayers with a monocrystalline domain larger than 1×1 cm² (see Supporting Information (SI), Section S1) were prepared on glass substrates via an air-water interface method as shown in Figure Then, reactive ion etchings (Trion Phantom III RIE/ICP) were performed to shrink the size of the PSNS to various smaller diameters D while maintaining their lattice spacing L (Figure 1b). The etched PSNS monolayer-coated substrates were loaded into a custom-built electron-beam deposition system and mounted on a substrate holder with one motor to control the polar rotation angle θ (the angle between the substrate surface normal and the vapor deposition

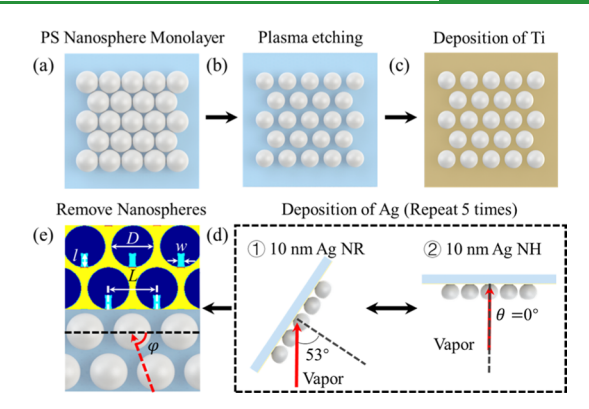


Figure 1. Fabrication scheme: (a) A PSNS monolayer with a diameter L=500 or 750 nm was formed on a clean glass slide; (b) the monolayer was O_2 plasma-etched to a smaller diameter D; (c) a 3 nm thick Ti thin film was deposited at $\theta=0^\circ$ followed by (d): ① 10 nm of Ag NR layer deposition ($\theta=53^\circ$) and ② 10 nm Ag NH layer deposition ($\theta=0^\circ$). Both steps ① and ② were repeated five times to form a 50 nm ACRH layer; (e) the top half of the image shows the ACRH structure after removing the PSNS layer with Scotch tape. The ACRH structure was predicted with an in-house MATLAB program. The bottom half of the image shows the definition of φ .

direction). The vacuum chamber was pumped down under a base pressure of <10⁻⁶ Torr, and the monolayer-coated substrates were positioned to face normally to the vapor deposition direction. The deposition rate and vapor thickness on the substrate were monitored by a quartz crystal microbalance facing the source. A 3 nm thick Ti layer was deposited to promote the adhesion of the subsequent Ag layer (Figure 1c). Ag nanostructures were prepared with a deposition configuration shown in Figure 1d. First, θ was changed to 53° to deposit NRs. To ensure that the vapor would pass through the gap between two adjacent nanospheres to form a NR structure on the substrate, a laser diffraction apparatus was used to align the monocrystalline monolayers (area > 1 cm²) in the direction of φ = 90°, φ is defined as the angle formed by a projection line of the incident vapor (red dashed arrow in Figure 1e) and an imaginary line that passes through the center of one row of PSNS (black-dashed line in Figure 1e) (see SI, Sections S2 and S3 for details). A 10 nm thick Ag layer was deposited at a deposition rate of 0.05 nm/s to form the NR structure. Then, another 10 nm thick Ag layer was deposited at θ = 0° to form the NH structure. These two steps were repeated five times to achieve a final Ag nanostructure thickness of 50 nm. Multiple depositions were used to increase the thickness of the deposited material incrementally (10 nm) to minimize the shadowing effects due to the films⁴⁰ previously deposited during NR fabrication. This deposition strategy also facilitated connectivity of the NRs and the NHs and ensured that the NHs were circular instead of elliptical (see SI, Section S4). The monolayer template was removed using Scotch tape after the Ag deposition, and the substrates were successively rinsed in toluene, acetone, and 2-propanol to remove PSNS residue.

Optical and Morphological Characterization. The morphology of the resultant ACRH structures was characterized by atomic force microscopy (AFM, Park Systems NX-10 AFM). The AFM images were analyzed using XEI software (XE Image Processing Program, XEI.Ink). The optical transmission spectra of the structures were measured with an ultraviolet—visible spectrophotometer (UV—vis, Jasco-750). A 40× objective lens was added between the incident light and sample surface to focus the incident light on a smaller area. Polarization-dependent spectra were achieved by adding a matched set of polarizers to the Jasco system via a home-built mounting and alignment system (see SI, Section S5).

Numerical Calculation. An in-house MATLAB program was used to predict the Ag pattern on the substrate based on the deposition configuration in Figure 1d.⁴¹ The program predicted the thickness distribution of the Ag film on the substrate by considering the shadowing effects from 36 nearest-neighbor PSNSs. An example

of a calculated NRinNH structure with L = 500 nm and D = 340 nm is shown in Figure 1e. The definitions of rod length l and width w, the diameter of the hole D (same as the diameter of the PSNS after etching), and the periodicity L (same as the original diameter of the PSNS before etching) are shown in Figure 1e.

A commercial software package (FDTD Solutions v 8.16.931, Lumerical Solutions Inc.) was used to calculate the transmission spectra $(T(\lambda))$ and electric field (*E*-field) distributions of the ACRH structures. The AFM images of the fabricated structures were used as the calculation models in the FDTD software. Two or three rectangular unit cells were set as the calculation area with periodic boundary conditions in the two lateral dimensions (see SI, Section S6). Perfectly matched layer boundary conditions were used on the top and bottom surfaces of the calculation domain. "Frequency-domain field and power" and "frequency-domain field profile" monitors were set up to determine the $T(\lambda)$ and *E*-field distributions, respectively. The optical parameters for the Ag and glass (SiO₂) substrates were taken from Palik's handbook.⁴²

■ RESULTS AND DISCUSSION

Effects of the Hole Size *D* on ACRH Structure Geometry. Figure 2a-f shows representative AFM images

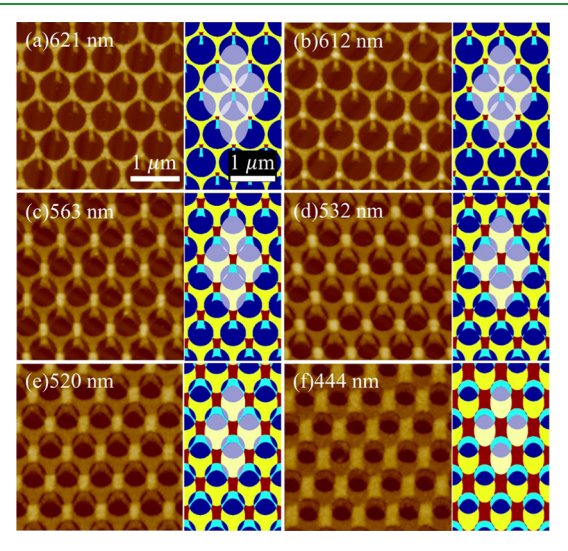


Figure 2. Representative AFM images and MATLAB calculations for the ACRH structures ($L=750~\mathrm{nm}$) with different PSNS etching time t and diameter D. (a) $t=400~\mathrm{s}$, $D=621~\mathrm{nm}$, (b) $t=500~\mathrm{s}$, $D=612~\mathrm{nm}$, (c) $t=600~\mathrm{s}$, $D=563~\mathrm{nm}$, (d) $t=650~\mathrm{s}$, $D=532~\mathrm{nm}$, (e) $t=700~\mathrm{s}$, $D=520~\mathrm{nm}$, and (f) $t=800~\mathrm{s}$, $D=444~\mathrm{nm}$. The white shaded areas in the calculated images show the elliptical shadows of four PSNS when $\theta=53^\circ$ and $\varphi=90^\circ$.

with L = 750 nm for monolayers etched at different t or with different D. The corresponding pattern calculated by MATLAB is in the immediate right to each AFM image, and the white shaded areas are the projected elliptical shadows generated by four adjacent nanospheres at $\theta = 53^{\circ}$. The NRs can only grow into the unshaded brown and cyan areas. As D decreases, one observes the evolution of three distinct patterns: D > 563 nm, connected NR in NH (NRinNH) structures (Figure 2a,b); 563 nm $\geq D \geq$ 520 nm, Y-shaped NR in NH (YinNH) structures (Figure 2c-e); and D < 520 nm, small elliptical NH structures (ENH) (Figure 2f). High-magnification AFM images and detailed analyses of morphology are presented in the SI, Section S7. As shown in Figure 2a,b, when D = 621 and 612 nm, the elliptical shadows of the adjacent spheres in the simulated patterns partly overlap and result in a well-separated, narrow, and nonshaded area. Thus, very thin

and well-defined NRs were formed inside the NHs as evidenced in AFM images. When D further decreased but remained >563 nm, the overlap area between the neighboring projected shadows decreased, the nonshaded area became larger, and w became wider while l decreased marginally. Figure S10a summarizes both *l* and *w* versus *D* extracted from AFM images. As D increases, l slowly increases while w decreases gently. Thus, the aspect ratio of the rod A = l/wincreases with increasing D, as shown in Figure S10b. The overlap area between the neighboring projected shadows decreased significantly when D decreased to 563 nm. Thus, the curved edge of the elliptical shadows as well as the spherical shape started to play an important role in the determination of the shape of the nonshaded area. Since the etched spheres preserved spherical shape, some deposited vapors were able to slip underneath the slightly overlapped projected shadows and formed a Y-shape at the tip of the NRs at $\theta = 53^{\circ}$ (Figure 2c, D = 563 nm). However, because the two Y-branches were formed through the deposition below the projected shadows, the tips were sharp. When D decreased to 532 nm, the projected shadows were tangent to each other, and two Y-branches with sharp tips were formed via a similar strategy. However, gaps formed between adjacent elliptical shadows when D decreased to 520 nm. The two branches of the Y-shape were determined by the gap, and the branches connected to the other edge of each NH. At this condition, it was expected that an elliptical NH array would be formed on top of the NH array. The structure was the overlap of two NH arrays; the bottom one was circular while the top was elliptical. When D = 444 nm, Figure 2f, one end of the projected elliptical shadow was tangent to the two neighboring circular NHs, and the nonshaded area covered almost half of the NH. Resultantly, the pattern was a smaller, elliptically shaped hole. In this case, the pattern can still be treated as the overlap of two NH arrays, similar to Figure 2e. From the AFM analysis in Figure S10c, we also noticed that the thickness of the NRs and NHs for all structures stayed almost unchanged ($h_R \approx 47 \pm 4$ nm for NRs and $h_{\rm H} \approx 50 \pm 1$ nm for NHs).

In addition to D, φ is another important factor that could strongly influence the final patterns. Figure S11 shows some calculated patterns for the same D but at different φ . As φ changed from 90 to 60°, the NRs gradually tilted and then finally connected to the edge of the NHs to form a grating-like structure. Therefore, two key factors are important to form large-area NRinNH structures: a large-area single domain PSNS monolayer and the azimuthal alignment of the domain orientation to the vapor deposition direction.

Polarization-Dependent Transmission Spectra $T(\lambda, \phi)$ and E_7 -Field Distributions. The representative polarization angle-dependent transmission spectra $T(\lambda,\phi)$ of the NRinNH structures are presented in Figure 3a,b. Here, the light incident angle is 0° and the polarization angle ϕ is defined as the angle between the polarization direction of the incident light and the long axis of NRs. In comparison, the $T_{\rm NH}(\lambda)$ of the pure NH arrays with the same L and D are also plotted as dashed curves in the corresponding figures. Their spectra were also summarized together in Figure S12 with corresponding AFM images. Regardless of the D, the $T_{\rm NH}(\lambda)$ spectra possess two EOT peaks (P₁ and P₂) caused by the surface plasmon resonance at the Ag-air and Ag-glass interfaces and two Wood's anomaly dips (D_1, D_2) , which are well characterized in the EOT community.⁴³ Compared to $T_{NH}(\lambda)$, the $T(\lambda,\phi)$ for the NRinNH structures show richer spectral features. The

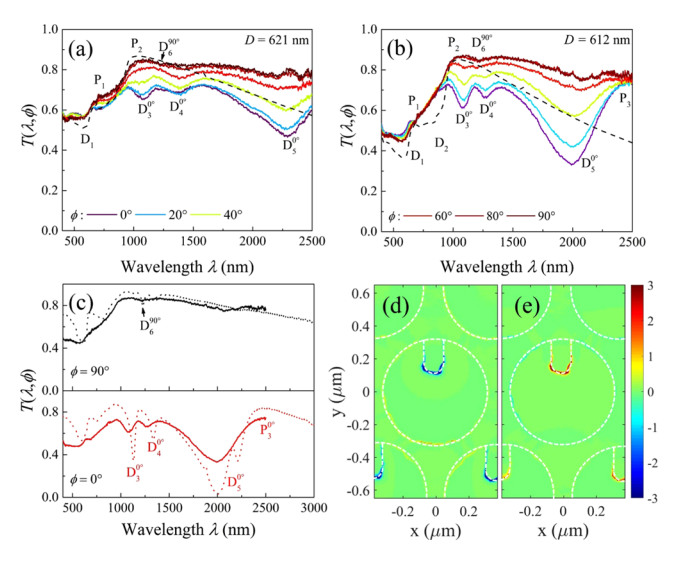


Figure 3. (a, b) are the $T(\lambda,\phi)$ of the NRinNH structures shown in Figure 2a,b, and the black-dashed curves are the $T_{\rm NH}(\lambda)$ of the corresponding NH array. (c) Comparison of the experimental (solid curves) and FDTD calculated $T(\lambda,\phi)$ (dashed curves) of the L=750 nm and D=612 nm NRinNH structure. (d) and (e) are the E_z -field distributions at λ_{P3} and $\lambda_{D_3^{0,0}}$ of (c) at the Ag–glass interface.

most notable difference is that the spectra show strong ϕ dependence due to broken symmetry. The trend for $T(\lambda,\phi)$ with different D is similar: (1) When $\phi = 0^{\circ}$, three dips, $D_3^{0\circ}$, $D_4^{0\circ}$, and $D_5^{0\circ}$, were observed in the broad wavelength region of P_2 in $T_{NH}(\lambda)$. (2) A new peak P_3 also appeared in the infrared wavelength region when $\phi = 0^{\circ}$. For D = 621 nm, P_3 appeared at a wavelength larger than 2500 nm, while for D = 612 nm, λ_{P3} blue-shifted to ~2450 nm. Though the addition of an NR in NH reduces the perforated ratio PR (PR = $1 - A_m/A_0$, where A_0 is the total area of the film and $A_{\rm m}$ is the metal covered area), i.e., the PR changes from 0.579 for the NH with D = 599to 0.511 nm for the NRinNH structure with D = 612 nm, the transmission T around λ_{P3} is highly increased when compared with that of $T_{NH}(\lambda)$. For example, T at $\lambda_{P3} = 2450$ nm increased from ~ 0.4 of $T_{\rm NH}(\lambda)$ to nearly 0.8, as shown in Figure 3b. Apparently, since the transmission enhancement F (= T/PR) at λ_{P3} for the NRinNH exceeds unit (1.47), the same as that of the NH at λ_{P2} , the P₃ peak should be noted as a new EOT mode. (3) When ϕ changed from 0 to 90°, the dips $D_3^{0\circ}$, $D_4^{0\circ}$, and $D_5^{0\circ}$ gradually disappeared and P_2 gradually recovered to a broad peak with a larger integrated transmission as the T around λ_{P3} remained almost unchanged. (4) When ϕ = 90°, a small dip (D_6) in the wavelength region of P_2 in $T_{\rm NH}(\lambda)$ appeared, and the overall $T(\lambda,90^{\circ})$ was similar to $T_{\rm NH}(\lambda)$ but with broader spectral features. Such wide-band and polarization-dependent properties can be applied to optical filters and polarization-modulation based optical components or sensors, respectively.

The spectral features in $T(\lambda,\phi)$ of the NRinNH structures also vary with D. Figure S13a,b directly compares the $T(\lambda,0^\circ)$ and $T(\lambda,90^\circ)$ for different D. The wavelengths of different resonances λ_0 are plotted against D in Figure S13c. As D increases, the $\lambda_{D_3^{0_\circ}}$, $\lambda_{D_4^{0_\circ}}$, and $\lambda_{D_5^{0_\circ}}$ red-shift: the $\lambda_{D_3^{0_\circ}}$ changes slowly, the $\lambda_{D_4^{0_\circ}}$ increases gradually, and the $\lambda_{D_5^{0_\circ}}$ red-shifts significantly.

To further understand the $T(\lambda,\phi)$ of the NRinNH structures, FDTD calculations were performed based on

representative AFM images. Figure 3c shows a comparison of the experimental (solid curves) and calculated (dashed curves) $T(\lambda,\phi)$ at $\phi=0$ and 90° for a D=612 nm sample, and the corresponding experimental and calculated peak and dip wavelengths are summarized in Table S1 in the SI Section S10. Overall, the calculated results agree with the experimental spectra except that the dips in the calculated spectra are sharper and stronger. At $\phi = 0^{\circ}$, except for an extra dip at $\lambda =$ 2208 nm, the spectral features of D_3^{00} , D_4^{00} , D_5^{00} , and P_3 are all well predicted by FDTD calculation. The additional small dip in the calculated results may be caused by imperfections of the selected AFM region used in the calculation. These imperfections were amplified by periodic boundary conditions in the calculation, and their effects on optical properties cannot be ignored. To better understand the origin of the spectral features, Figure 3d,e plots the local E_z -field distributions at the Ag-glass interface at $\lambda_{D_s^{0}}$. Based on discussions of similar structures in ref 15 and other references, 16,17,44 the new EOT peak P3 was induced by the coupling of the LSPR of the NR and an in-phase resonance of the rim of the NH, which is consistent with what is shown in Figure 3d: a strong dipole resonance of the NR and the high local electric field (the maximum $|E/E_0|^2 = 1077$ and the average $|E/E_0|^2 = 3.7$ over a unit cell) are demonstrated. In part, this also explains why the F at λ_{P3} exceeds unity for the NRinNH structure. Only a strong dipole resonance of the NR is evident for $\lambda_{D_s^{0_o}}$, as shown in Figure 3e. This implies that the dip is mainly caused by the LSPR of the NR, and weak coupling between the NR and the NH may exist. This result is also supported by the strong polarization dependence of $T(\lambda,\phi)$ at $\lambda_{D_s^{0}}$. In addition, the maximum and average field enhancement $|E/E_0|^2$ over a unit cell at different λ_0 are plotted in Figure S14. The $|E/E_0|^2$ at $\lambda_{D_s^0}$. shows the highest value, which indicates that the dip D_5 could be very useful for surface-enhanced spectroscopy or plasmonic sensors.

The dips $D_3^{0\circ}$ and $D_4^{0\circ}$ were different from P_3 and $D_5^{0\circ}$ since they appeared in the EOT peak (P2) of the NH array and correspond to a high energy resonance position, suggesting that they may be related to higher-order plasmon resonances (see SI, Section 10). It has been theoretically predicted that the higher-order resonances of a metal nanoring can be excited at normal incidence through asymmetric coupling with a nanodisk. 45,46 The excitation of higher-order modes is rationalized in terms of plasmon hybridization, 10,47 which adds a dipolar character to the multipolar modes and facilitates their coupling with the incident field. However, to date, the excitation of higher-order modes of the ring have been manifested indirectly as Fano-like interferences⁴⁸ when a multipolar resonance spectrally overlaps with broad dipolar resonance.⁴⁹ The E_z-field distribution shown in Figure S16a indicates that the resonance at $\lambda_{D_3^{0_\circ}}$ has an octupolar field distribution. This octupolar mode is induced by the asymmetric coupling of the NH with the dipole resonance of the NR along the long axis of the NR. The higher-order modes normally have narrow line shapes, and the resonance position of this octupolar mode is directly above the super-radiant SPP mode P_2 . Thus, the Fano-like dip $D_3^{0\circ}$ is the result of the interference between the narrow octupolar mode of the NHinNR and the super-radiant SPP mode in the compound hole array. The E_{τ} -field distribution at $D_4^{0\circ}$ shows coupling between the dipole mode of the NRs and another higher-order mode of the NHs, the hexapode mode, which is also induced by the asymmetric coupling of the NHs with dipole resonance of the NRs. Thus, $D_4^{0\circ}$ is the result of interference between the dipole—hexapode mode and the relatively wide SPP mode. Additionally, $D_3^{0\circ}$ shows stronger maximum and average $|E/E_0|^2$ than that of $D_4^{0\circ}$ (Figure S14) because $\lambda_{D_4^{0\circ}}$ is closer to λ_{P2} .

At $\phi=90^\circ$, both the calculated and experimental spectral exhibit a broad peak with a small dip at $\lambda_{D_6^{90_\circ}}=1220$ nm. The E_z -field distribution at $\lambda_{D_6^{90_\circ}}$ shown in Figure S16c demonstrates a bonding mode of dipole NRs and quadrupole NHs along the rod width direction. Based on the above discussion, $D_6^{90_\circ}$ is observed as a result of the destructive interference between the spectrally overlapping broad SPP resonance and the narrow dipole—quadrupole bonding mode of the NHinNRs.

For the YinNH structure (563 nm $\geq D > 520$ nm), the $T(\lambda, \phi)$ also depends strongly on ϕ , as shown in Figure 4a,b.

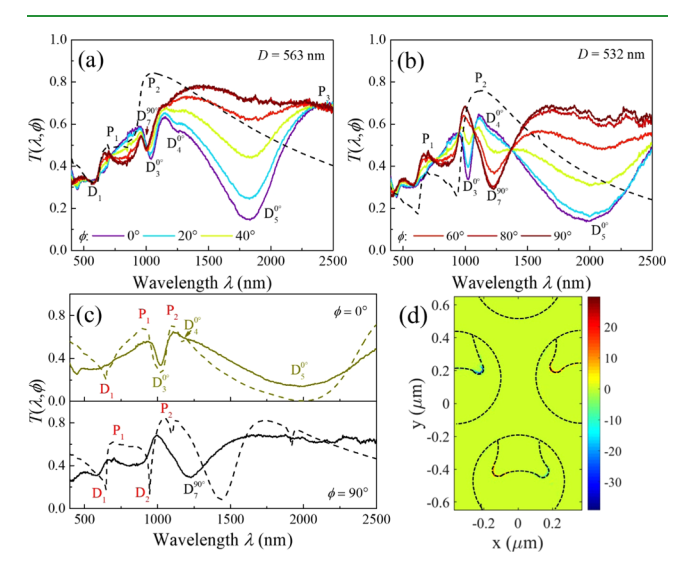


Figure 4. (a, b) are the $T(\lambda,\phi)$ of the YinNH structures shown in Figure 2c,d: the black-dashed curves are the $T_{\rm NH}(\lambda)$ of the corresponding NH array. (c) Comparison of the experimental (solid curves) and FDTD calculated (dashed curves) $T(\lambda,\phi)$ of the L=750 nm, D=532 nm YinNH structure shown in Figure 2d. (d) E_z -field distribution at $\lambda_{D_y^{0,0}}$ of (c) at the Ag-glass interface.

(1) At $\phi = 0^{\circ}$, the three dips, $D_3^{0\circ}$, $D_4^{0\circ}$, and $D_5^{0\circ}$, were observed on top of P2, and an EOT, peak P3 appeared. Unlike the spectral features of NRinNH structures, the dip $D_4^{0\circ}$ only appeared as a shoulder, and it almost merged into the spectral feature of $D_5^{0\circ}$, while the dip $D_3^{0\circ}$ became more pronounced and sharp. (2) When ϕ changes from 0 to 90°, the dips $D_3^{0\circ}$ $D_4^{0\circ}$, and $D_5^{0\circ}$ started to disappear while a new dip $D_7^{90\circ}$ appeared suddenly at $\phi \geq 30^{\circ}$, which could correspond to a resonant mode in the direction perpendicular to the long axis of the rods. When D decreased from 563 to 532 nm, $\lambda_{D_7^{90}}$ redshifted significantly from 1000 to 1222 nm. FDTD calculations were performed to probe the cause of D_7^{900} . The calculated $T(\lambda,\phi)$ of D=532 nm are shown in Figure 4c. The overall spectral shape of the calculated results agrees with that of the experimental results except for two small dips around $\lambda = 1100$ and 1900 nm when $\phi = 90^{\circ}$. These two extra dips were excited due to the use of the periodic boundary conditions of the imperfect AFM area as we mentioned previously. Similar to the spectra of NRinNH structures, the dips $D_3^{0\circ}$, $D_4^{0\circ}$, $D_5^{0\circ}$, and the peak P_3 have the same physical origins, but the dip $D_7^{90\circ}$ is

significantly different from the dip $D_6^{90\circ}$. The E_z -field distribution at $\lambda_{D_7^{90\circ}}$ at the Ag-glass interface shown in Figure 4d suggests a strong dipole resonance of the two branches of the "Y" rod along the light polarization direction. This resonance also occurs near P_2 ; thus, the dip $D_7^{90\circ}$ is caused by the interference of the dipole mode of the rods with the SPP mode of the NHs. This also explains the red shift of $\lambda_{D_7^{90\circ}}$ with decreasing D: the distance between the ends of the two Y-branches increased from ~180 to ~260 nm when D decreased from 563 to 532 nm, thus $\lambda_{D_7^{90\circ}}$ red-shifted.

In addition, the PR is 0.382 for the YinNH (D = 563 nm). This value is smaller than 0.491 for the NH with similar D (D= 552 nm) and 0.511 for the D = 612 nm NRinNH, but the Fis 1.84, which is significantly larger than F of the NH (1.70, D = 552 nm) and NRinNH (1.47, D = 612 nm) (see Table S2). The high F is due to two effects. First, regarding the conventional EOT phenomenon, the reduction of PR in NH array causes an increased F due to tunneling through surface plasmons. 50,51 As shown in Table S2, our experiment on NH arrays shows that the F at λ_{P2} increased from 1.38 to 2.03 when PR decreased from 0.628 to 0.325. Second, a strong localized E-field would further enhance the transmission since P3 originates from the localized plasmon resonance. Similar to the NRinNH structure, the large E-field enhancement $|E/E_0|^2$ at λ_{P3} for the D = 563 nm YinNH shown in Figure S17 indicates a strong localized surface plasmon resonance strength at λ_{P3} , which contributes to the high F (for a detailed discussion, see the SI, Section S11). The large electric field enhancement at λ_{P3} for the YinNH structures may be beneficial for sensing applications. The resonance positions of all of the peaks and dips and their causes are also summarized in Table S1 in the SI Section S10.

Figure 5 shows the typical ϕ -dependent $T(\lambda,\phi)$ of the ENH structure (D = 444 nm). The EOT peak P_3 vanished due to the

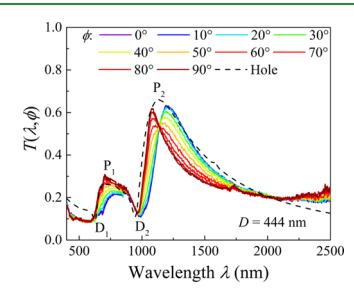


Figure 5. $T(\lambda,\phi)$ of the ENH structure shown in Figure 2f.

lack of strong localized resonance of the nanostructures inside the NHs. The $T(\lambda,\phi)$ is very close to the corresponding $T_{\rm NH}(\lambda)$ but with different EOT P_2 wavelengths when the incident light is parallel to the long axis (shorter wavelength) or short axis (longer wavelength) of the ENH, similar to plain elliptical NH arrays reported in the literature. ⁵²

To compare the overall polarization dependence $T(\lambda,\phi)$ of the three different structures, we plotted $T_{\rm DS}$ in polar coordinates in Figure 6 for different D. The dip $D_{\rm S}$ was chosen because $T_{\rm DS}$ not only represents the greatest difference in $T(\lambda,\phi)$ at different ϕ but also shows the highest local electric field. For the ENH structure, we plot $T(2000~{\rm nm},\phi)$ in Figure 6 as a reference. The polar plots of $T_{\rm DS}$ are dumbbell-shaped quadratic symmetric curves and show minimums of T at $\phi=0$ and 180° , indicating strong LSPR absorption along

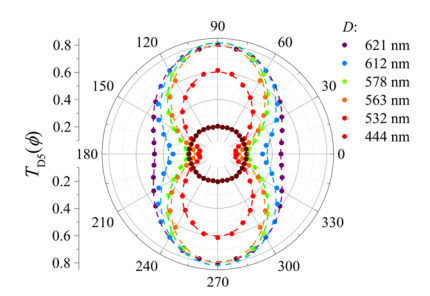


Figure 6. Polar plot of $T_{\rm DS}$ of different D. The dashed lines are sine square fitting results.

the NR direction regardless of structure (except for ENHs). Similar to previous studies for in-plane dipole mode resonance, $^{21,53-56}$ the polar plots of $T_{\rm DS}$ can be fitted well with squared cosine curves, $T=T_0-\alpha^{2*}\cos(\phi)^2$, where α is the polarizability of the long axis of the structure. The dashed curves shown in Figure 6 are the fitting results. As D decreased for the NRinNH structures (566 nm < D < 621 nm), $T(0^\circ)$ decreased while $T(90^\circ)$ stayed almost unchanged, thus $\Delta T=T(90^\circ)-T(0^\circ)$ gradually increased. The corresponding fitting parameters, (T_0,α^2) , are (0.79, 0.33) for D=621 nm, (0.82, 0.46) for D=612 nm, and (0.82, 0.60) for D=578 nm. Essentially, T_0 stays almost unchanged while α^2 decreases with D, thus, the ratio $\frac{T_0-\alpha^2}{T_0}$ increased monotonically with D. Notice that the smaller the $\frac{T_0-\alpha^2}{T_0}$ ratio, the stronger the ϕ -dependence. For the YinNH structures (520 nm < $D \leq 563$ nm), both $T(0^\circ)$ and $T(90^\circ)$ decreased with D, and the corresponding fitting parameters T_0 and α^2 are (0.80, 0.63) for

dependence. For the YinNH structures (520 nm < $D \le 563$ nm), both $T(0^{\circ})$ and $T(90^{\circ})$ decreased with D, and the corresponding fitting parameters T_0 and α^2 are (0.80, 0.63) for D = 563 nm and (0.60, 0.48) for D = 532 nm, i.e., the ratio $\frac{T_0 - \alpha^2}{T_0}$ almost remained ~0.2 when D changed. For the ENHs (D = 444 nm), $T(2000, \phi) = 0.211 - 0.008* \cos(\phi)^2$, i.e., $\frac{T_0 - \alpha^2}{T_0} \approx 0.96$, the ϕ -dependence was not significant.

The effect of L on the optical properties of ACRHs was also investigated, and the corresponding AFM images and $T(\lambda,\phi)$ at L = 500 nm with different D are shown in the SI, Section S12. Similar to when L = 750 nm, the overall morphology changes from NRinNH, to YinNH, then to ENH, and the $T(\lambda,\phi)$ showed similar ϕ -dependence with decreasing D. The main difference in optical properties is the absolution wavelengths λ_0 of the resonance features. Figure S21a shows a comparison of $T(\lambda,0^{\circ})$ and $T(\lambda,90^{\circ})$ for the NRinNH structures with the same D/L (\sim 0.8) ratio. Compared to samples at L=750 nm, the $T(\lambda,\phi)$ at L=500 nm possesses similar spectral features but with all of the resonance positions blue-shifted because of the reduction of L and D. The longer the wavelength of the resonance, the greater the blue shift. The dip $D_5^{0\circ}$ shows the largest blue shift among all of the visible resonances, from 2300 nm at L = 750 to 1360 nm at L = 500nm. The peak P_3 blue-shifted from >2500 to 1832 nm when L decreased from 750 to 500 nm. Figure S21b compares the YinNH spectra for L = 500 and 750 nm with the same D/L(~0.7) ratio. Trends similar to those shown in NRinNH structures are observed: the $T(\lambda,\phi)$ of L=500 nm possesses similar spectral features to those when L = 750 nm with all of the resonance positions blue-shifted. Since the peaks and dips all blue-shift with decreasing L, λ_{P3} is now within the measurement region, and a relatively complete peak shape

can be observed. This is beneficial for analyzing the influence of structure parameters on λ_{P3} . λ_0 of different D at L=500 nm when $\phi=0^\circ$ are summarized in Figure S22. We can see that λ_{P3} shows a high tunability: it can be tuned to red-shift from 1832 to 2218 nm when D decreases from 403 to 351 nm. The P_3 of YinNH structures have a longer resonance wavelength when compared to that of NRinNH structures because the two Y-branches increase the effective length of the NR.

Refractive Index Sensing Performance of the NRinNH and YinNH Structures to Be Used as an Index Sensor. One of the notable applications for NHs is refractive index sensing, 52,57-59 i.e., these structures can be used to sense the refractive index n change of their environment. Since the dip $D_5^{0\circ}$ possesses a strong local field enhancement (~7 and 2700 for the maximum and average $|E/E_0|^2$ in Figure S14), it is expected that this dip shows improved sensitivity. 36,60,61 The sensing performance of two typical ACRH structures, the NRinNH (L = 750 nm, D = 612 nm) and the YinNH (L = 750nm, D = 532 nm), has been characterized by immersing the samples in different organic solvents with indices of refraction varying from 1.36 to 1.50 (in SI, Section S13). Figure S24 shows the evolution of $T(\lambda, 0^{\circ})$ of the two samples for solvents with n = 1-1.50 and λ_0 versus n, where λ_0 was extracted from the experimental spectra by Fano-fitting 62-64 (details in SI, Section S13). All of the λ_0 -n relationships are linear, and the slope represents the refractive index sensitivity (RIS). D_5^{00} shows the fastest red shift and has the highest RIS among all of the resonances. The sensitivity of D_5^{00} of the YinNH structure is much higher (almost double) than that of the NRinNH structure. The improved sensitivity of $D_5^{0\circ}$ can be attributed to several reasons: first, the higher local field enhancement of YinNH when compared to that of NRinNH (SI, Section S11) helps to improve the sensitivity. Second, the increased sensing area of the YinNH structure enhances the sensitivity. The YinNH structure has more sensing area than that of the NRinNH, such that there is more interaction volume between the plasmonic structure and the dielectric environment. Finally, the dip $D_5^{0\circ}$ possesses the largest resonance wavelength λ_0 among all of the resonances. The positive relationship between λ_0 and the RIS is well-documented in Saison-Francioso et al.⁶⁵ and other literature reports.^{66–68} This is shown in Figure S26, where RIS is plotted as a function of λ_0 in

The new EOT peak P₃ possesses a larger resonance wavelength compared to that of dip D_5^{00} , and P_3 has both strong local field enhancement and high transmission, so it may provide another spectral characteristic for improved refractive index sensing. The sample with a smaller L (500 nm) was measured to investigate the RIS of the new EOT peak P_3^{00} , as shown in Figure 7a. Since the RIS of D_5^{00} for YinNH is higher than that of the NRinNH structure (Figure S24), we only measured the RI performance of the YinNH structure (D = 351 nm). All of the spectral features of $T(\lambda, 0^{\circ})$ red-shift substantially when n increases, as shown in Figure 7a. The resonance wavelengths versus *n* are plotted in Figure 7b. Based on linear fitting, the RIS of $D_5^{0\circ}$ is around 847 nm/RIU, which far exceeds the sensitivity of its corresponding pure NH sample shown in Figure S27. Due to the additional peaks caused by the molecular absorption of the solvents at $\lambda > 1500$ nm, λ_{P3}^{00} is only recognizable for one solvent. But based on the existing results, we can still estimate that the RIS of $P_3^{0\circ}$ is very high because λ_{P3}^{00} shifts from lower than 2000 nm to larger than 2500 nm within 0.5 unit change in n, indicating that the RIS of

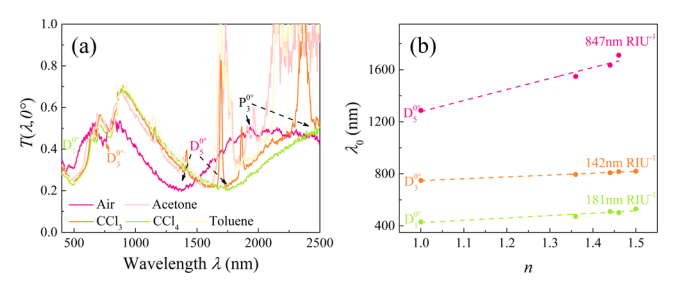


Figure 7. (a) $T(\lambda,0^\circ)$ of YinNH (L=500 nm, D=351 nm) samples in different solvents. (b) Plot of resonance positions of the dips and peaks in (a) versus n.

 $P_3^{0\circ}$ should be higher than 1000 nm/RIU. Further study of the sensitivity of P3 can be carried out using a smaller L to scale down the structure. The $T(\lambda,\phi)$ of the three samples used in the refractive index sensing experiments in different solvents are shown in the SI, Section S13.

In conclusion, adding NRs or Y-shaped NRs in the NH can highly improve the RIS of the NH array. It should also be noted that the samples used here for the refractive index sensing measurement were not optimal; better performance can be achieved if the structure parameters are carefully selected. The resonances with high sensitivity such as $D_5^{0\circ}$ and $P_3^{0\circ}$ can be tuned to the wavelength range of interest by adjusting the periodicity of the array. Utilizing the ϕ -sensitivity of the samples, further data processing can be applied to improve the figure of merit (FOM, calculated as RIS/FWHM, full width at half-maximum).

CONCLUSIONS

By encapsulating the unique merits of both NSL and OAD into one methodology, we find that asymmetric compound NH structures, including nanorod in nanohole, Y-shaped nanorod in nanohole, and elliptical nanohole, can be efficiently fabricated over large areas. The fabrication strategy described herein permits precise variation in the geometries of the formed compound nanostructure arrays, including the lattice periodicity, hole diameter, and rod length, by controlling the size of the PSNS, the etching duration of the PSNS, and the tilt angle during the metal layer deposition, respectively. The nanorod in nanohole and Y-shaped nanorod in nanohole structures possess a new EOT mode at the NIR region, which can be tuned to red-shift or blue-shift by D or L, and this feature offers a high degree of optical tunability. Taking advantage of the EOT, the tunable wavelength, as well as its polarization sensitivity, these structures may be efficacious substrates for near-perfect absorbers, bandpass filters, ^{69,70} or surface-enhanced Raman scattering spectroscopy. These results are important not only for understanding the interference of different plasmon modes in plasmonic systems but also for developing numerous plasmon-based optical and optoelectronic devices.

ASSOCIATED CONTENT

3 Supporting Information

The Supporting Information is available free of charge at https://pubs.acs.org/doi/10.1021/acsami.0c06936.

Quality of the PSNS monolayer; laser diffraction; determination of φ ; deposition procedure; transmission measurement setup; general setup of FDTD calculation; effect of the hole size D on the resulting ACRH

structures; effect of φ on the resulting ACRH structures; influence of structure parameters on optical properties; causes of all of the resonances in Figures 3c and 4c; comparison of transmission enhancement between NRinNH and YinNH structures; influence of array periodicity on morphology and optical responses; refractive index sensing experiments (PDF)

AUTHOR INFORMATION

Corresponding Authors

Zhengjun Zhang — Key Laboratory of Advanced Materials (MOE) and School of Materials Science and Engineering, Tsinghua University, Beijing 100084, P. R. China;

orcid.org/0000-0001-8727-6373; Email: zjzhang@tsinghua.edu.cn

Yiping Zhao — Department of Physics and Astronomy, University of Georgia, Athens, Georgia 30602, United States; o orcid.org/0000-0002-3710-4159; Email: zhaoy@uga.edu

Authors

Yanfeng Wang — Key Laboratory of Advanced Materials (MOE) and School of Materials Science and Engineering, Tsinghua University, Beijing 100084, P. R. China; Department of Physics and Astronomy, University of Georgia, Athens, Georgia 30602, United States; orcid.org/0000-0001-7698-6230

Harrison B. Chong — Department of Physics and Astronomy, University of Georgia, Athens, Georgia 30602, United States; orcid.org/0000-0003-0880-089X

Complete contact information is available at: https://pubs.acs.org/10.1021/acsami.0c06936

Author Contributions

The manuscript was written through the contributions of all authors. All authors have given approval to the final version of the manuscript.

Notes

The authors declare no competing financial interest.

ACKNOWLEDGMENTS

Y.W. and Z.Z. were financially supported by the Basic Science Center Project of NSFC under Grant No. 51788104 and the Chinese National Natural Science Foundation (51761145045 and 51531006). H.B.C. and Y.Z. were financially supported by the National Science Foundation under Grant No. ECCS-1808271. Y.W. was also supported by the program of China Scholarships Council (No. 201806210308).

ABBREVIATIONS

EOT, extraordinary optical transmission NR, nanorod NH, nanohole ACRH, asymmetric compound NRinNH NRinNH, NR in NH YinNH, Y-shaped NR in NH ENH, elliptical NH structures LSPR, localized surface plasmon resonance SPP, surface plasmon polaritons FDTD, finite difference time domain NSL, nanosphere lithography PSNS, polystyrene nanospheres OAD, oblique angle deposition

PR, perforated ratio

REFERENCES

- (1) Huang, W.-x.; Wang, Q.-j.; Yin, X.-g.; Huang, C.-p.; Huang, H.; Wang, Y.-m.; Zhu, Y.-y. Optical Resonances in a Composite Asymmetric Plasmonic Nanostructure. *J. Appl. Phys.* **2011**, *109*, No. 114310.
- (2) He, M.-D.; Liu, J.-Q.; Wang, K.-J. Transmission Resonances in a Symmetry-Broken Square Coaxial Aperture in a Metal Film. *J. Phys. D: Appl. Phys.* **2012**, *45*, No. 345304.
- (3) Zhang, F.; Huang, X.; Zhao, Q.; Chen, L.; Wang, Y.; Li, Q.; He, X.; Li, C.; Chen, K. Fano Resonance of an Asymmetric Dielectric Wire Pair. *Appl. Phys. Lett.* **2014**, *105*, No. 172901.
- (4) Melentiev, P. N.; Afanasiev, A. E.; Kuzin, A. A.; Baturin, A. S.; Balykin, V. I. Subwavelength Light Localization Based on Optical Nonlinearity and Light Polarization. *Opt. Lett.* **2013**, *38*, 2274–2276.
- (5) Zhang, S.; Li, G. C.; Chen, Y.; Zhu, X.; Liu, S. D.; Lei, D. Y.; Duan, H. Pronounced Fano Resonance in Single Gold Split Nanodisks with 15 nm Split Gaps for Intensive Second Harmonic Generation. ACS Nano 2016, 10, 11105–11114.
- (6) Melentiev, P. N.; Afanasiev, A. E.; Kuzin, A. A.; Gusev, V. M.; Kompanets, O. N.; Esenaliev, R. O.; Balykin, V. I. Split Hole Resonator: A Nanoscale UV Light Source. *Nano Lett.* **2016**, *16*, 1138–1142.
- (7) Melentiev, P. N.; Afanasiev, A. E.; Kuzin, A. A.; Baturin, A. S.; Balykin, V. I. Giant Optical Nonlinearity of a Single Plasmonic Nanostructure. *Opt. Express* **2013**, *21*, 13896–13905.
- (8) Li, L.; Liang, Y.; Peng, W.; Liu, Y. Fano-like Resonances in the Binary Elliptical Nanoring Resonator Array. *Opt. Mater. Express* **2018**, *8*, 2131–2139.
- (9) Luk'yanchuk, B.; Zheludev, N. I.; Maier, S. A.; Halas, N. J.; Nordlander, P.; Giessen, H.; Chong, C. T. The Fano Resonance in Plasmonic Nanostructures and Metamaterials. *Nat. Mater.* **2010**, *9*, 707–715.
- (10) Zhao, K.; Huo, Y.; Liu, T.; Li, J.; He, B.; Zhao, T.; Liu, L.; Li, Y. Manipulation of Electrical Field Enhancements and Fano Resonances in Nanoellipsoid/Ring Plasmonic Cavities. *Plasmonics* **2015**, *10*, 1041–1048
- (11) Chen, Z.; Li, P.; Zhang, S.; Chen, Y.; Liu, P.; Duan, H. Enhanced Extraordinary Optical Transmission and Refractive-Index Sensing Sensitivity in Tapered Plasmonic Nanohole Arrays. *Nanotechnology* **2019**, *30*, No. 335201.
- (12) Liu, Q.; Song, Y.; Zeng, P.; Zhang, C.; Chen, Y.; Wang, H.; Luo, Y.; Duan, H. High-Fidelity Fabrication of Plasmonic Nanoholes Array via Ion-Beam Planarization for Extraordinary Transmission Applications. *Appl. Surf. Sci.* **2020**, *526*, No. 146690.
- (13) Wu, S.; Wang, Q.-j.; Yin, X.-g.; Li, J.-q.; Zhu, D.; Liu, S.-q.; Zhu, Y.-y. Enhanced Optical Transmission: Role of the Localized Surface Plasmon. *Appl. Phys. Lett.* **2008**, *93*, No. 101113.
- (14) Wang, C.; Gu, J.; Han, J.; Xing, Q.; Tian, Z.; Liu, F.; Chai, L.; Li, Y.; Hu, M.; Wang, Q.; Lu, X.; Zhang, W. Role of Mode Coupling on Transmission Properties of Subwavelength Composite Hole-Patch Structures. *Appl. Phys. Lett.* **2010**, *96*, No. 251102.
- (15) Wang, Y.; Luong, H.; Zhang, Z.; Zhao, Y. Coupling between Plasmonic Nanohole Array and Nanorod Array: the Emerging of a New Extraordinary Optical Transmission Mode and Epsilon-Near-Zero Property. J. Phys. D: Appl. Phys. 2020, 53, No. 275202.
- (16) Larson, S.; Luong, H.; Song, C.; Zhao, Y. Dipole Radiation-Induced Extraordinary Optical Transmission for Silver Nanorod-Covered Silver Nanohole Arrays. *J. Phys. Chem. C* **2019**, *123*, 5634–5641.
- (17) Li, Z.-B.; Zhou, W.-Y.; Kong, X.-T.; Tian, J.-G. Polarization Dependence and Independence of Near-Field Enhancement through a Subwavelength Circle Hole. *Opt. Express* **2010**, *18*, 5854–5860.
- (18) Tognalli, N. G.; Fainstein, A.; Calvo, E. J.; Abdelsalam, M.; Bartlett, P. N. Incident Wavelength Resolved Resonant SERS on Au Sphere Segment Void (SSV) Arrays. *J. Phys. Chem. C* **2012**, *116*, 3414–3420.

- (19) Yoo, D.; Mohr, D. A.; Vidal-Codina, F.; John-Herpin, A.; Jo, M.; Kim, S.; Matson, J.; Caldwell, J. D.; Jeon, H.; Nguyen, N. C.; Martin-Moreno, L.; Peraire, J.; Altug, H.; Oh, S. H. High-Contrast Infrared Absorption Spectroscopy via Mass-Produced Coaxial Zero-Mode Resonators with Sub-10 nm Gaps. *Nano Lett.* **2018**, *18*, 1930–1936
- (20) Cai, H.; Meng, Q.; Zhao, H.; Li, M.; Dai, Y.; Lin, Y.; Ding, H.; Pan, N.; Tian, Y.; Luo, Y.; Wang, X. High-Throughput Fabrication of Ultradense Annular Nanogap Arrays for Plasmon-Enhanced Spectroscopy. ACS Appl. Mater. Interfaces 2018, 10, 20189–20195.
- (21) Cooper, C. T.; Rodriguez, M.; Blair, S.; Shumaker-Parry, J. S. Polarization Anisotropy of Multiple Localized Plasmon Resonance Modes in Noble Metal Nanocrescents. *J. Phys. Chem. C* **2014**, *118*, 1167–1173.
- (22) Balykin, V. I.; Melentiev, P. N. Optics and Spectroscopy of a Single Plasmonic Nanostructure. *Phys.-Usp.* **2018**, *61*, 133–156.
- (23) Melentiev, P. N.; Afanasiev, A. E.; Kuzin, A. A.; Baturin, A. S.; Balykin, V. I. Giant Optical Nonlinearity of a Single Plasmonic Nanostructure. *Opt. Express* **2013**, *21*, 13896–13905.
- (24) Commandré, M.; Vial, B.; Tisserand, S.; Roux, L.; Dallaporta, H.; Bedu, F.; Demésy, G.; Nicolet, A.; Zolla, F. Design, Fabrication and Characterization of Resonant Metamaterial Filters for Infrared Multispectral Imaging. *Thin Solid Films* **2015**, *592*, 296–304.
- (25) Hou, R.; Shynkar, V.; Lafargue, C.; Kolkowski, R.; Zyss, J.; Lagugne-Labarthet, F. Second Harmonic Generation from Gold Meta-Molecules with Three-Fold Symmetry. *Phys. Chem. Chem. Phys.* **2016**, *18*, 7956–7965.
- (26) Huang, L.; Chen, X.; Muhlenbernd, H.; Li, G.; Bai, B.; Tan, Q.; Jin, G.; Zentgraf, T.; Zhang, S. Dispersionless Phase Discontinuities for Controlling Light Propagation. *Nano Lett.* **2012**, *12*, 5750–5755. (27) Li, W.; Coppens, Z. J.; Besteiro, L. V.; Wang, W.; Govorov, A.
- O.; Valentine, J. Circularly Polarized Light Detection with Hot Electrons in Chiral Plasmonic Metamaterials. *Nat. Commun.* **2015**, *6*, No. 8379.
- (28) de Waele, R.; Burgos, S. P.; Polman, A.; Atwater, H. A. Plasmon Dispersion in Coaxial Waveguides From Single-Cavity Optical Transmission Measurements. *Nano Lett.* **2009**, *9*, 2832–2837.
- (29) Jiang, X.; Gu, Q.; Wang, F.; Lv, J.; Ma, Z.; Si, G. Fabrication of Coaxial Plasmonic Crystals by Focused Ion Beam Milling and Electron-Beam Lithography. *Mater. Lett.* **2013**, *100*, 192–194.
- (30) Kessentini, S.; Barchiesi, D.; D'Andrea, C.; Toma, A.; Guillot, N.; Di Fabrizio, E.; Fazio, B.; Maragó, O. M.; Gucciardi, P. G.; Lamy de la Chapelle, M. Gold Dimer Nanoantenna with Slanted Gap for Tunable LSPR and Improved SERS. *J. Phys. Chem. C* **2014**, *118*, 3209–3219.
- (31) Liu, Y. J.; Si, G. Y.; Leong, E. S.; Xiang, N.; Danner, A. J.; Teng, J. H. Light-Driven Plasmonic Color Filters by Overlaying Photoresponsive Liquid Crystals on Gold Annular Aperture Arrays. *Adv. Mater.* **2012**, *24*, OP131–OP135.
- (32) Wang, S.; Dong, H.; Sun, F.; Zhang, W.; Liang, Y.; Tian, L.; Wang, P.; Yin, X.; Li, G. Large-Area Fabrication of Highly Tunable Hybrid Plasmonic—Photonic Structures Based on Colloidal Lithography and a Photoreconfigurable Polymer. *Adv. Opt. Mater.* **2019**, *7*, No. 1900483.
- (33) Colson, P.; Henrist, C.; Cloots, R. Nanosphere Lithography: A Powerful Method for the Controlled Manufacturing of Nanomaterials. *J. Nanomater.* **2013**, 2013, 1–19.
- (34) Chegel, V. I. Nanostructured Materials for Biosensor Applications: Comparative Review of Preparation Methods. In *Manipulation of Nanoscale Materials*; RSC, 2012; Chapter 13, pp 318–355.
- (35) Zheng, P.; Cushing, S. K.; Suri, S.; Wu, N. Tailoring Plasmonic Properties of Gold Nanohole Arrays for Surface-Enhanced Raman Scattering. *Phys. Chem. Chem. Phys.* **2015**, *17*, 21211–21219.
- (36) Zheng, P.; Li, M.; Jurevic, R.; Cushing, S. K.; Liu, Y.; Wu, N. A Gold Nanohole Array Based Surface-Enhanced Raman Scattering Biosensor for Detection of Silver(I) and Mercury(II) in Human Saliva. *Nanoscale* **2015**, *7*, 11005–11012.

- (37) Hawkeye, M. M.; Taschuk, M. T.; Brett, M. J. Glancing Angle Deposition of Thin Films_Engineering the Nanoscale Engineering the Nanoscale; Wiley, 2014.
- (38) Kosiorek, A.; Kandulski, W.; Chudzinski, P.; Kempa, K.; Giersig, M. Shadow Nanosphere Lithography: Simulation and Experiment. *Nano Lett.* **2004**, *4*, 1359–1363.
- (39) Ingram, W. M.; Han, C.; Zhang, Q.; Zhao, Y. Optimization of Ag-Coated Polystyrene Nanosphere Substrates for Quantitative Surface-Enhanced Raman Spectroscopy Analysis. *J. Phys. Chem. C* **2015**, *119*, 27639–27648.
- (40) He, Y.; Wang, X.; Ingram, W.; Ai, B.; Zhao, Y. Optimized Fan-Shaped Chiral Metamaterial as an Ultrathin Narrow-Band Circular Polarizer at Visible Frequencies. *Nanotechnology* **2018**, 29, No. 165301.
- (41) Larsen, G. K.; He, Y.; Ingram, W.; Zhao, Y. Hidden Chirality in Superficially Racemic Patchy Silver Films. *Nano Lett.* **2013**, *13*, 6228–6232.
- (42) Palik, E. D. Handbook of Optical Constants of Solids; Academic Press: Orlando, FL, 1985.
- (43) Wood, R. W. Anomalous Diffraction Gratings. Phys. Rev. 1935, 48, 928–936.
- (44) Yue, W.; Wang, Z.; Yang, Y.; Li, J.; Wu, Y.; Chen, L.; Ooi, B.; Wang, X.; Zhang, X. X. Enhanced Extraordinary Optical Transmission (EOT) through Arrays of Bridged Nanohole Pairs and Their Sensing Applications. *Nanoscale* **2014**, *6*, 7917–7923.
- (45) Hao, F.; Sonnefraud, Y.; Dorpe, P. V.; Maier, S. A.; Halas, N. J.; Nordlander, P. Symmetry Breaking in Plasmonic Nanocavities: Subradiant LSPR Sensing and a Tunable Fano Resonance. *Nano Lett.* **2008**, *8*, 3983–3988.
- (46) Fu, Y. H.; Zhang, J. B.; Yu, Y. F.; Luk'yanchuk, B. Generating and Manipulating Higher Order Fano Resonances in Dual-Disk Ring Plasmonic Nanostructures. *ACS Nano* **2012**, *6*, 5130–5137.
- (47) Yang, D.-J.; Yang, Z.-J.; Li, Y.-Y.; Zhou, L.; Hao, Z.-H.; Wang, Q.-Q. Tunable Fano Resonance in Rod-Ring Plasmonic Nanocavities. *Plasmonics* **2015**, *10*, 263–269.
- (48) Habteyes, T. G.; Dhuey, S.; Cabrini, S.; Schuck, P. J.; Leone, S. R. Theta-Shaped Plasmonic Nanostructures: Bringing "Dark" Multipole Plasmon Resonances into Action via Conductive Coupling. *Nano Lett.* **2011**, *11*, 1819–1825.
- (49) Verellen, N.; Sonnefraud, Y.; Sobhani, H.; Hao, F.; Moshchalkov, V. V.; Dorpe, P. V.; Nordlander, P.; Maier, S. A. Fano Resonances in Individual Coherent Plasmonic Nanocavities. *Nano Lett.* **2009**, *9*, 1663–1667.
- (50) Rodrigo, S. G. Extraordinary Optical Transmission. In *Optical Properties of Nanostructured Metallic Systems*; Springer, 2012; pp 37–75.
- (51) Martín-Moreno, L.; Garcia-Vidal, F. J.; Lezec, H. J.; Pellerin, K. M.; Thio, T.; Pendry, J. B.; Ebbesen, T. W. Theory of Extraordinary Optical Transmission through Subwavelength Hole Arrays. *Phys. Rev. Lett.* **2001**, *86*, 1114–1117.
- (52) Ai, B.; Basnet, P.; Larson, S.; Ingram, W.; Zhao, Y. Plasmonic Sensor with High Figure of Merit Based on Differential Polarization Spectra of Elliptical Nanohole Array. *Nanoscale* **2017**, *9*, 14710–1472.1
- (53) Huang, Y.; Kim, D. H. Dark-Field Microscopy Studies of Polarization-Dependent Plasmonic Resonance of Single Gold Nanorods: Rainbow Nanoparticles. *Nanoscale* **2011**, *3*, 3228–3232.
- (54) Itoh, T.; Biju, V.; Ishikawa, M.; Kikkawa, Y.; Hashimoto, K.; Ikehata, A.; Ozaki, Y. Surface-Enhanced Resonance Raman Scattering and Background Light Emission Coupled with Plasmon of Single Ag Nanoaggregates. *J. Chem. Phys.* **2006**, *124*, No. 134708.
- (55) Wei, H.; Hao, F.; Huang, Y.; Wang, W.; Nordlander, P.; Xu, H. Polarization Dependence of Surface-Enhanced Raman Scattering in Gold Nanoparticle-Nanowire Systems. *Nano Lett.* **2008**, *8*, 2497–2502.
- (56) Ming, T.; Zhao, L.; Yang, Z.; Chen, H.; Sun, L.; Wang, J.; Yan, C. Strong Polarization Dependence of Plasmon-Enhanced Fluorescence on Single Gold Nanorods. *Nano Lett.* **2009**, *9*, 3896–3903.

- (57) Cervantes Tellez, G. A.; Ahmed, A.; Gordon, R. Optimizing the Resolution of Nanohole Arrays in Metal Films for Refractive-Index Sensing. *Appl. Phys. A: Mater. Sci. Process.* **2012**, *109*, 775–780.
- (58) Lesuffleur, A.; Im, H.; Lindquist, N. C.; Oh, S.-H. Periodic Nanohole Arrays with Shape-Enhanced Plasmon Resonance as Real-Time Biosensors. *Appl. Phys. Lett.* **2007**, *90*, No. 243110.
- (59) van der Molen, K. L.; Segerink, F. B.; van Hulst, N. F.; Kuipers, L. Influence of Hole Size on the Extraordinary Transmission through Subwavelength Hole Arrays. *Appl. Phys. Lett.* **2004**, *85*, 4316–4318.
- (60) Jain, P. K.; El-Sayed, M. A. Noble Metal Nanoparticle Pairs: Effect of Medium for Enhanced Nanosensing. *Nano Lett.* **2008**, *8*, 4347–4352.
- (61) Lassiter, J. B.; Aizpurua, J.; Hernandez, L. I.; Brandl, D. W.; Romero, I.; Lal, S.; Hafner, J. H.; Nordlander, P.; Halas, N. J. Close Encounters between Two Nanoshells. *Nano Lett.* **2008**, *8*, 1212–1218
- (62) Fan, W.; Zhang, S.; Minhas, B.; Malloy, K. J.; Brueck, S. R. Enhanced Infrared Transmission through Subwavelength Coaxial Metallic Arrays. *Phys. Rev. Lett.* **2005**, *94*, No. 033902.
- (63) Chang, S.-H.; Gray, S. K.; Schatz, G. C. Surface Plasmon Generation and Light Transmission by Isolated Nanoholes and Arrays of Nanoholes in Thin Metal Films. *Opt. Express* **2005**, *13*, 3150–3165
- (64) Meierott, S.; Hotz, T.; Neel, N.; Kroger, J. Asymmetry Parameter of Peaked Fano Line Shapes. *Rev. Sci. Instrum.* **2016**, 87, No. 103901.
- (65) Saison-Francioso, O.; Lévêque, G.; Boukherroub, R.; Szunerits, S.; Akjouj, A. Dependence between the Refractive-Index Sensitivity of Metallic Nanoparticles and the Spectral Position of Their Localized Surface Plasmon Band: A Numerical and Analytical Study. *J. Phys. Chem. C* 2015, 119, 28551–28559.
- (66) Larson, S.; Zhao, Y. Localized Surface Plasmonic Resonance and Sensing Properties of Ag–MgF2 Composite Nanotriangles. *J. Phys. Chem. C* **2018**, *122*, 7374–7381.
- (67) Miller, M. M.; Lazarides, A. A. Sensitivity of Metal Nanoparticle Surface Plasmon Resonance to the Dielectric Environment. *J. Phys. Chem. B* **2005**, *109*, 21556–21565.
- (68) Miller, M. M.; Lazarides, A. A. Sensitivity of Metal Nanoparticle Plasmon Resonance Band Position to the Dielectric Environment as Observed in Scattering. *J. Opt. A: Pure Appl. Opt.* **2006**, *8*, S239—S249.
- (69) Yoon, J.; Zhou, M.; Badsha, M. A.; Kim, T. Y.; Jun, Y. C.; Hwangbo, C. K. Broadband Epsilon-Near-Zero Perfect Absorption in the Near-Infrared. *Sci. Rep.* **2015**, *5*, No. 12788.
- (70) Halterman, K.; Elson, J. M. Near-Perfect Absorption in Epsilon-Near-Zero Structures with Hyperbolic Dispersion. *Opt. Express* **2014**, 22, 7337–7348.